

# **Polymer infiltrated ceramic networks with biocompatible adhesive and 3D-printed highly porous scaffolds**

*Ludmila Hodasova,<sup>1,2,3</sup> Jordi Sans,<sup>1,3</sup> Brenda G. Molina,<sup>1,3</sup> Carlos Alemán,<sup>1,3,4</sup> Luis Llanes,<sup>2,3</sup> Gemma Fargas,<sup>2,3\*</sup> Elaine Armelin<sup>1,3\*</sup>*

<sup>1</sup> Departament d'Enginyeria Química, Universitat Politècnica de Catalunya, Campus Diagonal Besòs (EEBE), C/ Eduard Maristany, 10-14, Building I, 2nd floor, 08019, Barcelona, Spain.

<sup>2</sup> Departament de Ciència i Enginyeria de Materials, Universitat Politècnica de Catalunya, Campus Diagonal Besòs - EEBE, C/ Eduard Maristany, 10-14, Building I, 1st floor, 08019, Barcelona, Spain.

<sup>3</sup> Barcelona Research Center for Multiscale Science and Engineering, Universitat Politècnica de Catalunya, Campus Diagonal Besòs (EEBE), C/ Eduard Maristany, 10-14, Building I, basement floor, 08019, Barcelona, Spain.

<sup>4</sup> Institute for Bioengineering of Catalonia (IBEC), The Barcelona Institute of Science and Technology, Baldiri Reixac 10-12, 08028 Barcelona, Spain.

*Corresponding authors:* [elaine.armelin@upc.edu](mailto:elaine.armelin@upc.edu) and [gemma.fargas@upc.edu](mailto:gemma.fargas@upc.edu)

## Abstract

Herein, for the first time is described the design of a novel porous zirconia scaffolds manufactured by using polymer-infiltrated ceramic network (PICN) and 3D-printing technologies. Cubic geometry of pieces was obtained by perpendicular layer-by-layer deposition of yttrium-stabilized tetragonal zirconia polycrystal (3Y-TZP) and Pluronic<sup>®</sup> hydrogel ceramic paste. The specimens were prepared by robocasting assembly with 50% infill and 50% of pores, as feed setup. Bisphenol A glycerolate dimethacrylate (Bis-GMA) and tri(ethylenglycol) dimethacrylate (TEGDMA) copolymer, a well-known biocompatible adhesive, which is widely used in dentistry field, was employed to reinforce the pores of the 3D-printed ceramic structure. The success of the acrylate polymer infiltration above the scaffold surface and among the 3Y-TZP filaments was achieved through previous ceramic functionalization with 3-(trimethoxysilyl)propyl methacrylate ( $\gamma$ -MPS). The well infiltration of the material on pores was evaluated by gravimetry, obtaining a value of  $87.5 \pm 6.6$  % of pores covered by the adhesive. Such successful infiltration of methacrylate copolymer had also a positive effect on the mechanical properties of the scaffold material, being the PICN sample that one with the highest elongation resistance. The new system showed reduced bacteria proliferation, over 24h of incubation with Gram-negative *Escherichia coli* and Gram-positive *Streptococcus salivarius* bacteria lines, when compared to the control.

**Keywords:** Robocasting; yttrium stabilized zirconia; acrylate polymer; bacteria colonization

## 1. Introduction

Nowadays, 3D-printing is a well-established and suitable technology for the dentistry industry [1,2]. The range of dental devices that can be processed with 3D printing technologies is wide, including teeth restorations, dental appliances, orthodontic and prosthodontic models, dentures, orthodontic splints, dental trays and utensils, surgical guides, crowns and bridges, among others [3–8].

Within the above context, some companies have been specialized in the design and fabrication of sophisticated 3D-printers for the dental market (e.g. 3D Systems Inc., EnvisionTEC Inc., Stratasys Ltd., and others). The availability of such speedy printers together with advanced software are transforming the dental field. A number of healthcare companies have launched their commercial activity based on additive manufacturing (NextDent B.V., Hybrid Technologies USA, Glidewell Laboratories Inc., etc). Several production methods are available, such as selective laser sintering (SLS),[9] direct metal printing (DMP),[10] selective laser melting (SLM),[11] stereolithography (SLA)[12][13] and digital light processing (DLP),[14][15][16] among others [4,5,17]. In this sense, robocasting process allows the obtaining of dental pieces without shape restrictions, high dimensional precision, smooth finishing, efficiency, repeatability and cost effectiveness [18,19].

Although, lots of different classes of materials are being used for 3D-printing technologies[20–25], among them, ceramic compounds are the most widely used for dentistry applications. The most important classes in biomedical field are alumina ( $\alpha$ - $\text{Al}_2\text{O}_3$ ), spinel ( $\text{MgAl}_2\text{O}_4$ ) and zirconia ( $\text{ZrO}_2$ ) [26]. Yttrium-stabilized zirconia (YSZ) [27] has shown a great promise in many challenging situations (for example, in single-tooth restoration and long-span bridges) due to its advantageous properties with respect to other dental materials, such as the excellent aestheticism (brightness, refraction,

colouring finishing), chemical resistance, improved mechanical behavior compared to alumina and spinel (bending strength and fracture toughness), high ionic conductivity, low thermal conductivity at high temperature together with relatively high thermal expansion coefficient, and high thermal stability of degradation-resistance [5,28].

Despite its excellent properties, the major shortcoming of YSZ material is the low resistance to crack growth compared to metal implants, *i.e.* it behaves as a brittle material when subjected to impacts. Depending on the fabrication method and sintering temperature, the mechanical properties of zirconia varies substantially (fracture toughness ~25-60 GPa, flexural strength ~ 150-250 MPa, elastic modulus ~ 200-220 GPa).[29][30] Aiming to overcome this drawback and driven by the demands to design restorations with a real tooth-like function, fracture toughness and flexural strength of YSZ have been improved by following several approaches. For example, Srigurunathan *et al.* [31] have explored the benefits of doping ZrO<sub>2</sub> powder with rare-earth elements on the mechanical and optical properties of this material for biomedical applications. On the other hand, polymer-infiltrated-ceramic-network (PICN) materials have emerged in recent years, inspired by the glass-infiltrated ceramic [32] structures [33–36]. Pioneering work developed by Li *et al.* [30] demonstrated an enhanced mechanical performance improvement of polymer-infiltrated zirconia ceramics using bisphenol A glycerolate dimethacrylate (Bis-GMA) and tri(ethylenglycol) dimethacrylate (TEGDMA) prepared by conventional solid state ceramic process. Resistance to crack extension was substantially increased, as compared to the one exhibited by the porous zirconia ceramic precursors. Thus, the infiltrated polymer acted as the plasticizers do in polymer transformation, reducing the rigidity of the matrix.

Unfortunately, ceramic computer aided printing is easier for solid substrates pieces than for porous scaffold designs. This is mainly due to the weight of ceramic compounds

that may lead to bowing of filaments after the deposition and, therefore, user dissatisfaction. To overcome these problems, the direct-write assembly of materials with fugitive inks, developed by Lewis and co-workers[37,38], and nowadays commonly referred to robocasting or robotic direct deposition of ink filament, is a suitable option to retain both the shape of the scaffolds during fabrication and the dimensional stability of the ceramic filaments after sintering process.

From all of the above-mentioned aspects, we can conclude that it is extremely difficult to obtain porous architectures from ceramic inks with additive manufacturing. Once the filaments are sintered at high temperature, they usually break or deform. In this work, we were able to prepare stable 3D ceramic scaffolds by controlling several printer parameters (nozzle diameter, deposition speed, ink concentration) and by adding a polymer adhesive to reduce the stress of the scaffold filaments. For it, a strategy of zirconia surface functionalization with 3-(trimethoxysilyl)propyl methacrylate[39,40], was useful to the covalent adhesion of the biocompatible acrylate polymer. The idea of PICN fabrication with direct polymer infiltration aims to create a dental implant with superior properties, such as long lifespan, mechanical properties mimicking natural enamel and dentin to reduce mandibular bone stiffness, easy fabrication with possibility of personalized design, and ceramic-polymer interface without bacterial growth and adhesion promotion. Until now, PICN studies have been addressed with solid YSZ samples, which porosity changes uniquely depends on the sintering temperature and fabrication method (hot-pressing or cold-isostatic pressing). The novelty of the present work relies on the obtaining of a well-controlled scaffold arrangement by establishing a pre-fixed porosity, for the polymer infiltration, with the help of 3D-printing advanced equipment.

The properties of the whole scaffold will depend on the piece geometry, surface modification, porosity, among other parameters. Furthermore, zirconia crowns have been used as an alternative to the common gold, alumina and lithium disilicate crowns as well, and is due, in part, to its excellent antimicrobial behaviour compared to the formers [41][42]. However, the surface modification and geometry of biomaterial scaffolds will affect both the growth and adhesion of bacteria commonly found in oral cavity [43]. Thus, a detailed material characterization is necessary, as well as the investigation of the influence of such aspects on its microbial activity. The success of dental restoration therefore will be due to the success of avoiding biofilm formation.

The forecast growth of digital dentistry was calculated to be 23.2 % from 2018 to 2023, and it will represent a global market of 5.06 billion USD by 2023; which justify the need of more investigations on this field [14,15,44].

## **2. Experimental procedure**

### **2.1. Materials**

3Y-TZP (3 mol% yttrium- stabilized tetragonal zirconia polycrystal) with an average particle size of 300 nm (measured by SEM) and ceramic density of  $6.05 \text{ g}\cdot\text{cm}^{-3}$ , was provided by SEPR Saint-Gobain ZirPro under the commercial name CY3Z-R. The theoretical value of ceramic density (CY3Z-R grades) was taken from technical datasheet available on Saint-Gobain website. Pluronic® F-127 hydrogel;  $\gamma$ -MPS (3-(trimethoxysilyl)propyl methacrylate); Bis-GMA (bisphenol A glycerolate dimethacrylate); TEGDMA (triethylene glycol dimethacrylate) and BPO (benzoyl peroxide, Luperox® A75,) were all provided by Sigma-Aldrich.

For antimicrobial activity assays, Gram-negative *Escherichia coli* (*E. coli*) and Gram-positive *Streptococcus salivarius* (*S. salivarius*) bacteria lines were used. The other reagents employed for the bacteria culture media growth will be described in the section 2.5.

## 2.2. 3D-printed ceramic samples manufacturing

Porous zirconia structures were prepared from 25% Pluronic® F-127 hydrogel (25% w/w of Pluronic and 75% w/v of water) and 3Y-TZP powder at 30:70 weight ratio, respectively. They were 3D-printed by robocasting method (Figure 1 a-b) at Saint-Gobain Research Provence (France), employing a 3D Dima Elite dispenser (Nordson Dima, Netherlands) equipped with DimaSoft CAD/CAM software. Zirconia scaffolds were printed as  $1.5 \times 1.5 \times 1.0 \text{ cm}^3$  cubes with 50% infill of zirconia using a 800  $\mu\text{m}$  cylindrical nozzle for extrusion of ceramic paste from a syringe (Figure 1a), subsequently dried for 2 days in a chamber with controlled relative humidity of 90%, and for 2-3 days at 45% humidity chamber. Afterwards, a two-stage sintering process at 700°C and 1450°C, during 1h and 2h respectively (Figure 1c), was applied to obtain a stable tetragonal composition of zirconia particles. The heating and cooling temperature rates has been kept constant and equals to 3 °C/min. During the sintering process ~20 % shrinkage occurs within specimens' dimensions due to the degradation of the Pluronic® hydrogel and ceramic compactness, as will be discussed in the results section.

## 2.3. Dip-coating method to obtain the polymer-infiltrated ceramic networks (PICN)

Here, for a good swelling and adhesion of the polymeric adhesive to the 3D-printed ceramic samples composed by aligned filaments and macropores, a simple surface modification strategy was employed: (i) activation of the zirconia surface with silane coupling agent, and (ii) *in-situ* copolymerization of methacrylate polymer. The ceramic scaffolds were carefully cleaned by immersion in distilled water, by subsequently dipping in ethanol solvent (96%), and drying through air flow. In parallel, a solution of  $\gamma$ -MPS (24 mmol of liquid silane in 100 mL of 3:1 ethanol:water volume ratio) was prepared and left under magnetic stirring, for 1 h, for the silane hydrolysis. Afterwards, the 3D-printed

zirconia samples were submerged in such solution for 1 h, removed and left them wring thoroughly to eliminate the excess of liquid.

For the obtaining of Bis-GMA/TEGDMA copolymer, with molar ratio of 40:60 wt. %, covalently bonded to the 3D-printed zirconia cubes, the following procedure is exemplified. Previously to the immersion of the samples, a viscous solution of 39.5 wt. % Bis-GMA, 59.5 wt. % TEGDMA and 1.0 wt. % of BPO, as initiator, was prepared. The monomers were weighted in an analytical balance. Due to the high viscous property of Bis-GMA, the total amount of TEGDMA was adjusted to complete 99 wt. %. The catalyst amount was maintained constant. The whole system was stirred for 1 h at room temperature to start the copolymerization reaction. After the radical polymerization initiation, the silane-activated pieces were immersed for 1 h in the methacrylate viscous solution. Then, samples were carefully removed from the solution, the excess of liquid was left to drain, and the pieces were placed in a glass petri dish, covered with aluminum foil, before transfer to the oven. The complete polymerization reaction was carried out by placing the samples in a JP Selecta Vaciotem-T vacuum oven, during 10 h at 115°C (Figure 1d). Subsequently, the 3D-printed PICN samples were cleaned with distilled water and ethanol before they were used for characterization studies. Two more molar ratios of Bis-GMA and TEGDMA were also prepared with the same procedure: 30:70 wt. % and 50:50 wt. %. For the quantification of the amount of copolymer infiltrated, the samples were weight before and after the final process. All of the above-mentioned compositions were characterized by FTIR and Raman spectroscopies as well as by thermal analysis. Finally, the 40:60 Bis-GMA/TEGDMA copolymer was further investigated with XPS and Raman confocal analyses. In addition, bacterial cultures were conducted to assess its antimicrobial activity.

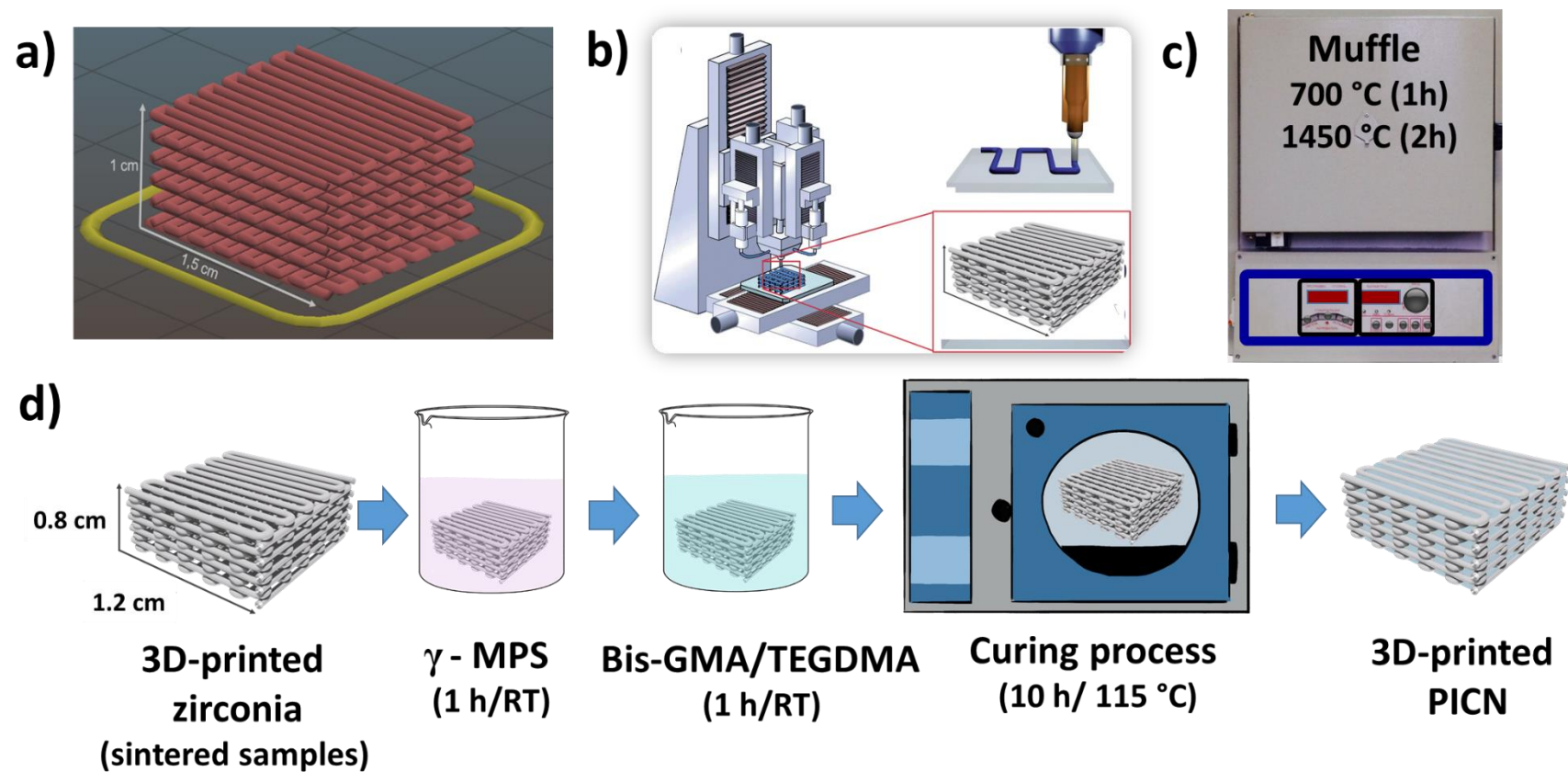


**Figure 1.** (a) DimaSoft CAD/CAM 3D design of simple cubic geometry (zig-zag filament layer-by-layer deposition and number of layers =10) of 3Y-TZP paste printing with 50% infill of zirconia. (b) Illustration of an ink-jet printer, filament deposition and the 3D-printed cubic specimen (Adapted from references [37,38]). (c) Sintering process with two stepwise heating, employing muffle furnace. (d) Sequential steps for the functionalization and copolymer deposition onto 3D-printed ceramic samples used in the present study.

## 2.4. Physical-chemical characterization

In order to evaluate the chemical structure of all PICN samples, from the silane surface functionalization to the copolymer-infiltrated samples, spectroscopy (FTIR-ATR, micro-Raman and XPS) and thermal analyses were performed. FTIR-ATR and thermal characterizations are described in the electronic supporting information (ESI).

The chemical structure of the  $\gamma$ -MPS monolayer was evaluated using XPS due to the nanometric dimensions of the film. The equipment used was a SPECS system equipped with a high intensity twin anode X-ray source XR50 of Mg/Al (1253 eV/1487 eV), operating at 150 W, placed perpendicular to the analyser axis, and using a Phoibos 150 MCD-9 XP detector. The spectra were recorded with a pass energy of 25 eV in 0.1 eV steps, for the survey and narrow scans, at a pressure below  $6 \times 10^{-9}$  mbar. As the internal reference, C 1s peak with a binding energy of 284.8 eV was used. The atomic percentage of each element was determined by dividing the peak area of the most intense XPS signal of each element by the corresponding sensitivity factor, and expressing it as a fraction of the sum of all normalized peak areas. High resolution XPS spectra were acquired by Gaussian/Lorentzian curve, fitting after S-shape background subtraction, for the following elements: C 1s, O 1s, Si 2p and Zr 3d.

The scaffold porosity ( $P_{scaffold}$ ) of each sample was calculated by dividing the scaffold's weight ( $m_{scaffold}$ ) by the theoretical weight of a scaffold with 100% infill ( $m_{theoretical}$ ):

$$P_{scaffold} = \left(1 - \frac{m_{scaffold}}{m_{theoretical}}\right) \times 100 \quad (\text{Eq. 1})$$

The scaffold's theoretical weight ( $m_{theoretical}$ ) was determined by density equation using the density of material ( $6.05 \text{ g/cm}^3$ ) and the volume of the scaffold was calculated from dimensions of the sample. Up to five mass measurements were taken to determine the porosity of the 3D-printed zirconia scaffold, with 50 % of hollow structure, using a

Mettler Toledo analytical balance (maximum capacity 81/120 g, repeatability  $\pm 0.01/0.1$  mg).

The success of polymer infiltration (I) into the pores was calculated with the following equation:

$$I = \left( \frac{m_{PICN}}{m_{PICN(T)}} \right) \times 100 = \left( \frac{m_{PICN}}{\rho_{PICN(E)} \times V_{PICN}} \right) \times 100 \quad (\text{Eq. 2})$$

where  $m_{PICN}$  is the weight of PICN composite and  $m_{PICN(T)}$  is the theoretical weight of PICN specimen with 100% pores infiltrated. The later, in turn, was calculated from the experimental density ( $\rho_{PICN(E)}$ ) of composite and volume ( $V_{PICN}$ ) of composite determined from dimension measurements. The experimental density of composite ( $\rho_{PICN(E)}$ ) was individually determined for each sample using the density of zirconia and the density of the copolymer (1.18 g/cm<sup>3</sup>), according to the equation 3:

$$\rho_{PICN(E)} = \left( 1 - \frac{P_{scaffold}}{100} \right) \times \rho_{zirconia} + \frac{P_{scaffold}}{100} \times \rho_{Copolymer} \quad (\text{Eq. 3})$$

The experimental density of the zirconia filaments was measured by using a gas displacement pycnometer (Micrometrics Instrument Co., model AccuPyc 1330). The equipment determines density and volume with pressure change of helium atmosphere in a vial with calibrated volume. Afterwards, the density is calculated by dividing weight by measured volume of a sample.

Raman spectra and 3D-mapping images of 3D-printed zirconia with infiltrated polymer network were obtained using Renishaw's inVia Qontor Raman microscope and Raman Environment (Wire™) software. The spectrometer is equipped with a Leica DM2700 M microscope for confocal measurements and LifeTrack technology for rough

and curved surfaces. The spectra were recorded in the range of 4000-100  $\text{cm}^{-1}$  and with a source of 532 nm, due to the hybrid nature of the whole implant model.

Morphology characterization and proper infiltration of polymer into zirconia structure were observed by SEM using a Focused Ion Beam Zeiss Neon 40 instrument, commercialized by Carl Zeiss (Germany). In order to avoid electron discharge, samples were carbon-coated using Mitek K950 Sputter Coater before analysis. The accelerating voltage for obtaining morphology micrographs was 2 kV. The side part of the copolymer infiltrated samples was appropriately polished by hand with silica carbide sandpapers, gradually evolving from P 600 to P 2500 level of abrasion before the analysis, to obtain a smooth surface for the observation of polymer-ceramic interface. SEM was also employed to observe the bacterial colonies formed on the surface of PICN hybrid material, after antibacterial activity experiments (section 2.5).

Compression strength was measured while undergoing compression test performed by Instron 8511 compression machine, with maximum load of 10 kN. The implied pressure rate for the experiment was 0.5 mm/s and the overall maximum pressure applied was ~7 kN. The results are represented as stress-strain curves.

## **2.5. Antibacterial activity**

To evaluate the antimicrobial activity, the bacteria adhesion and growth of two different lines, have been investigated in the presence of zirconia 3D-printed scaffolds, zirconia 3D-printed scaffolds with  $\gamma$ -MPS coating, and PICN hybrid material with a composition of 40:60 Bis-GMA/TEGDMA copolymer. Within this context, *Escherichia coli* (*E. coli*) and *Streptococcus salivarius* (*S. salivarius*), as Gram-negative and Gram-positive microorganisms, respectively, were employed. The bacteria were grown aerobically in Luria-Bertani (LB) broth culture (10 g/L tryptone, 5 g/L yeast extract, 5 g/L NaCl, pH 7.2) in advance,  $7 \times 10^9$  colony-forming units (CFU) per mL being seeded

in 10 mL LB broth medium after 24h. For antimicrobial assays,  $7 \times 10^9$  of CFU/mL were seeded in sterile vials containing the specimens and fresh 10 mL of LB broth. For the control sample, bacteria were cultured in a sterile vial without the presence of any additional material. Both sample lines, including control samples, were stored and incubated for 24 h at 37°C and 90 rpm. Then, turbidity of the solutions was analysed using UV absorbance, 200  $\mu$ L of bacteria solution for all the samples was placed in a 96-well plate and measure at  $\lambda = 595$  nm in a microplate reader (EZ Read 400– Biochrom, UK) with ADAP 2.0 Plus Data Analysis Software.

A similar procedure was utilized for bacteria adhesion assays. However, after seeding the samples in fresh LB broth for 24 h, they were lightly washed with distilled water and incubated again for 24h, before counting. The counting was carried out by UV spectroscopy, employing the same procedure described above. The absorbance data were then compared with the control, which were prepared with  $7 \times 10^9$  of CFU/mL seeded in sterile vials containing fresh 10 mL of LB broth without specimens.

The results of both experiments (*i.e.* antimicrobial activity and adhesion) are expressed in terms of relative cell viability to the control, and the average of 3 replicates of each type of a sample was performed with both bacteria lines. Statistical analyses were performed with a confidence level of 95% ( $p < 0.05$ ) using the Student's T-test.

Confocal laser scanning microscopy (LSM), which was performed using a Carl ZEISS LSM 800 equipment capable of performing epifluorescence techniques, was employed to observe bacteria coloured with blue fluorescent dye (Hoechst 33342).

### **3. Results and discussion**

#### **3.1. 3D-printing of yttrium-stabilized tetragonal zirconia ceramic with high porosity**

3D-printed cubes with controlled height, width and length, as well as controlled hollow structure were successfully extruded by robocasting manufacturing after the optimization of the printer trials (Figure 2a). Filaments were printed layer-by-layer in perpendicular fashion, creating a grid like structure, with macropores (Figure 2b). Those macropores imparted high porosity to the ceramic scaffold, allowing better penetration of polymeric resins in comparison to the classical method of PICN with polymer inside micropores. As commonly occurs, after the sintering process from 700°C to 1450°C, the samples lose about 20 % of the original printed dimensions, being the final size  $1.2 \times 1.2 \times 0.8 \text{ cm}^3$ . Due to this variation of samples dimensions and scaffold pore size, the proper ratio of Bis-GMA and TEGMA monomers was adjusted for the full infiltration of the copolymer inside the ceramic devices. A representative example of the PICN pieces with the copolymer film with 50:50 wt. % of Bis-GMA/TEGDMA composition is displayed in Figure 2c.

The major drawback of the 3D-printing process was the effective control of the mixture viscosity, which is highly dependent on the temperature and relative humidity of the mixture and printer rooms. By maintaining both parameters constant, it was possible to obtain reproducible pieces. Another relevant aspect to be taken into consideration was the printer head. Using a nozzle of 800  $\mu\text{m}$  of diameter, homogenous filaments diameter ( $704 \pm 22 \mu\text{m}$ ), pore sizes ( $422 \pm 45 \mu\text{m}$  wide) and dimensional stability of the whole piece were reached. Despite such parameters were well controlled, the printed ceramic samples with 50% infill configuration had slightly larger base than top dimensions upon drying and sintering processes, as can be seen from the photograph taken of one piece (Figure 2d, lateral view). It should be noted that, among over 25 printed pieces, few samples (2-3) had some irregular edges and non-homogenous porosity. However, when

using smaller nozzle (580  $\mu\text{m}$ ), the dimensional integrity was completely lose (Figure S1, ESI).

Gravimetric measurements are the most direct method of determining the porosity of solid materials. The experimental value for the scaffold porosity was calculated by gravimetry, taking into account the density of zirconia after sintering. The value found was  $5.86 \pm 0.08 \text{ g/cm}^3$ , which represents 97 % of the theoretical value. The proper polymer infiltration, after the adhesive curing reaction, was also measured by gravimetry. The free scaffold percentage obtained was practically equivalent to that fixed in the printer setup ( $49.98 \pm 2.75 \%$ ), confirming the good control offered by the advanced printer equipment and robocasting setup. After the polymer infiltration, it decreases substantially and, practically all the empty space is filled by the biocompatible adhesive. The success of polymer infiltration obtained was  $87.5 \pm 6.6 \%$  (Table S1). By contrary, such percentage of polymer in composite materials is not possible to find by conventional methods. As for example, Li *et. al.* [30] obtained 34.7-46.3 % of porosity after conventional cold-isostatic pressing and sintering process at temperatures varying from 1000 to 1150  $^{\circ}\text{C}$ . The higher the sintering temperature, the lower porosity was recorded, and therefore, a smaller number of pores were infiltrated. The Bis-GMA/TEGDMA copolymer content achieved, after the infiltration, varied from 12.3% to 18.4%, suggesting that the infiltration of such viscous copolymer is easier with bigger pores. In a recently published review, Bobbert and Zadpoor [45] highlighted the importance to control pore size, porosity, and fibre orientation in synthetic bone biomedical implants, like autografts, allografts and xenografts. Such critical parameters affect cell seeding efficiency, cell viability, cell proliferation and cell differentiation. In this work, by employing the robocasting technology, the porosity of specimens, the pore sizes and the ceramic filament diameter were designed prior to the ceramic manufacture, and all those

critical parameters were conserved after sintering. We have demonstrated that the pores were successfully filled with the methacrylate copolymer (Figures 2c-d) and thus, we have obtained the PICN hybrid material. Therefore, the present work represents advantage key advance with respect to the state-of-art in PICN technologies. The final properties of the resulting hybrid material are expected to be better controlled in comparison with those obtained using conventional methods.

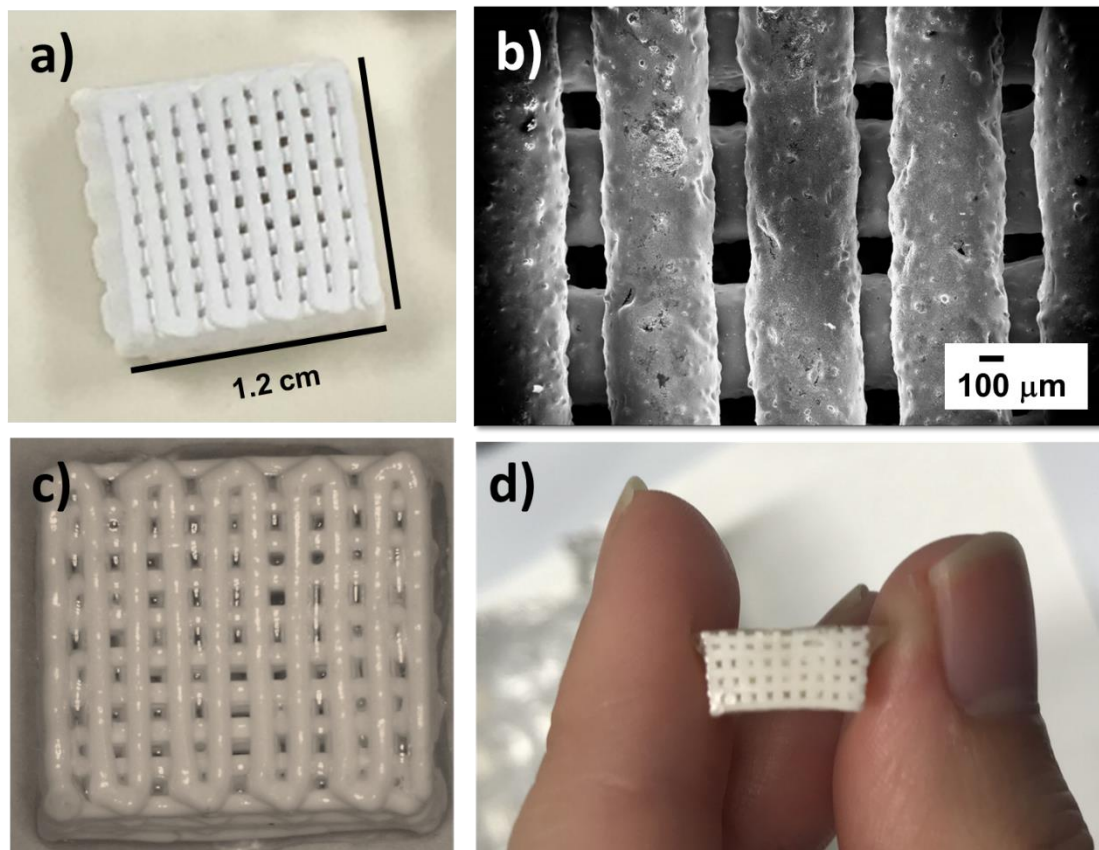
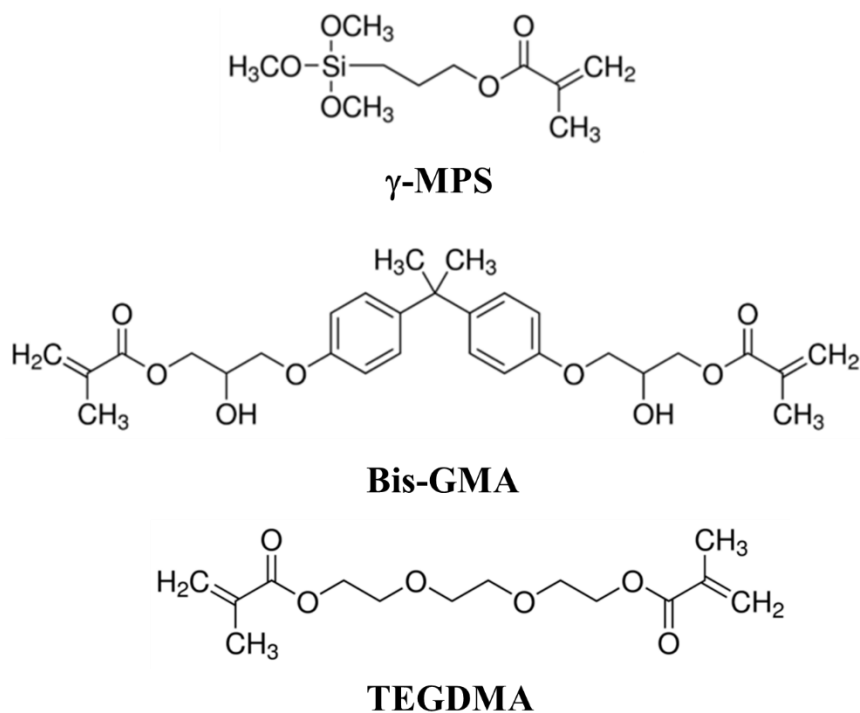


**Figure 22.** (a) Photograph of 3D-printed zirconia cube with stable dimensionality and pores formation upon drying and sintering processes. (b) SEM micrograph of zirconia filaments after printing and sintering processes. (c) Photograph of one PICN cube with 50 wt. % filled of 40:60 Bis-GMA/TEGDMA copolymer (gloss aspect over the filaments and inside the pores represents the copolymer coating and filling materials). (d) Photograph of 3D-printed ceramic with Bis-GMA/TEGDMA copolymer (lateral view).

### 3.2. Chemical structure and adhesion of the interpenetrating-polymer network to the 3D-printed ceramic devices

The use of silanization as a process to promote the further deposition and covalent bonding of other layers onto metal surfaces has been extensively reported [46–48]. Moreover, organosilane compounds in silica-based ceramics have also been extensively explored and, indeed, the organic-inorganic layer represents a good interface for the further deposition of other coatings [39,47,49]. However, silanization studies on zirconia-based ceramics are scarce and, typically, the silane content over zirconia is inferior to those observed for glass substrates. Caravaca *et al.* [50] have recently reported that the covalent bonding of 3-aminopropyltrimethoxy silane (APDMES), directly on the surface of zirconia (3Y-TZP), was promoted after sample surface cleaning with cold plasma treatment. In such study, the aim was to enhance stability and biointegration of zirconia with the osteoblast-like cells, as an optimization process to obtain biologically compatible dental implants with enhanced biointegration.

Although the adherence of methacrylate polymers is usually good (*i.e.* they have been used as main component in adhesive applications for many years, including dentistry adhesive bonding by photopolymerization), the failure of adhesion has several clinical implications [51]. In the present study, silanization of zirconia has been employed to transform the inert sintered zirconia surface into a functionalized one, and to actuate as coupling agent for the covalent bonding between Bis-GMA/TEGDMA copolymer and the porous ceramic cubic prototype to prolong the stability of the adhesive layer over time. For this purpose,  $\gamma$ -MPS was chosen as the coupling agent since it forms a stable monolayer with ceramic and metal surfaces, and it is the most used organosilane compound reported for dentistry applications [52]. The presence of terminal carbon-carbon double-bond groups is intended to help the copolymerization with Bis-GMA and TEGDMA monomers, during the radical polymerization steps (Scheme 1).



**Scheme 1.** Chemical structures of organosilane ( $\gamma$ -MPS) and monomers (Bis-GMA and TEGDMA) used for the zirconia functionalization and the preparation of the infiltrated polymer network, respectively.

The presence and successful application of  $\gamma$ -MPS to zirconia scaffold was detected by XPS analyses. In order to obtain a better understanding of the chemical bonds established after the polymerization reaction, all three modified surfaces of PICN manufacture were analyzed: zirconia scaffolds (3D-printed samples), zirconia scaffolds with  $\gamma$ -MPS silane layer, and zirconia scaffolds with silane monolayer and Bis-GMA/TEGDMA copolymer. Figure 3a represents the XPS high-resolution spectra of 3D-printed zirconia sample after sintering. As it can be seen, two main peaks of Zr–O bonds appear at 181.5 eV and 183.9 eV, corresponding to Zr 3d 5/2 and 3d 3/2 orbitals from ZrO<sub>2</sub> structures [53].

A great difference on the Zr 3d binding energies was observed for samples with the  $\gamma$ -MPS layer (Figure 3b), which exhibited a shift of +1.13 eV with respect to the pure 3Y-TZP that was attributed to the creation of new Zr–O–Si bonds on the ceramic surface

[54]. The Si 2p and O 1s XPS high resolution spectra confirm the well-established covalent linkages of Zr–O–Si in the ceramic-silane interface and the Si–C in the interface of silane-copolymer (Figure 3). Figure 3c represents the binding energies for 3D-printed sample with silane coating, where the peak at 99.1 eV was attributed to Zr–O–Si bonds [54] and the peak at 102.4 eV was assigned to Si–O–Si, which corresponds to the core of  $\gamma$ -MPS molecules [50,55]. The detection of Si–O–Si bonds, with higher intensities than those of Zr–O–Si linkages, suggest that an organosilane network is formed on the surface of the 3D-printed zirconia.

For the copolymer infiltrated sample (PICN), the two peaks obtained for Si 2p orbitals (Figure 3d) represent uniquely the linkages of  $\gamma$ -MPS with Bis-GMA/TEGDMA structure (Si–C, 104.0 eV) [56], and silane network (Si–O–Si, 102.0 eV) [50,57]. Si–C peak is quite wide and cannot be distinguished, in case it also covers other Si–O bonds (for example, Si–OH or Si–O–C from hydrolyzed and methylated silane, respectively). Moreover, atomic concentration data show that the amount of silane detected for the hybrid ceramic-resin sample (PICN scaffolds) is significantly lower than the amount detected over zirconia functionalized with  $\gamma$ -MPS silane layer (1.15 % and 9.18 %, respectively; Table S2).

The establishment of Zr–O–Si linkages on silanized 3D-printed zirconia samples can also be explained when evaluating the O 1s orbital. Pristine sample showed O 1s deconvoluted peaks at 527.5 eV, 529.1 eV and 530.5 eV, which are mainly associated with Y–O, Zr–O and O–H bonds, respectively (Figure 3e). After silanization, to the intensity of the peaks associated to the Zr–O and O–H bonds (529.1 eV and 530.3 eV, respectively) decreases and a new linkage related to Si–O–Si siloxane bonds appears at 531.4 eV (Figure 3f) [58]. The PICN surface presents little variation on O1s neighborhood, where much higher contribution of C–O–C/O–H, C–O/C=O bonds (532.6

eV, Figure 3g), belonging to the methacrylate copolymer (Bis-GMA/TEGDMA) coating, was achieved and less Si–O–C bonds were detected [59]. The high-resolution spectra of C 1s were reported in Figure S2.

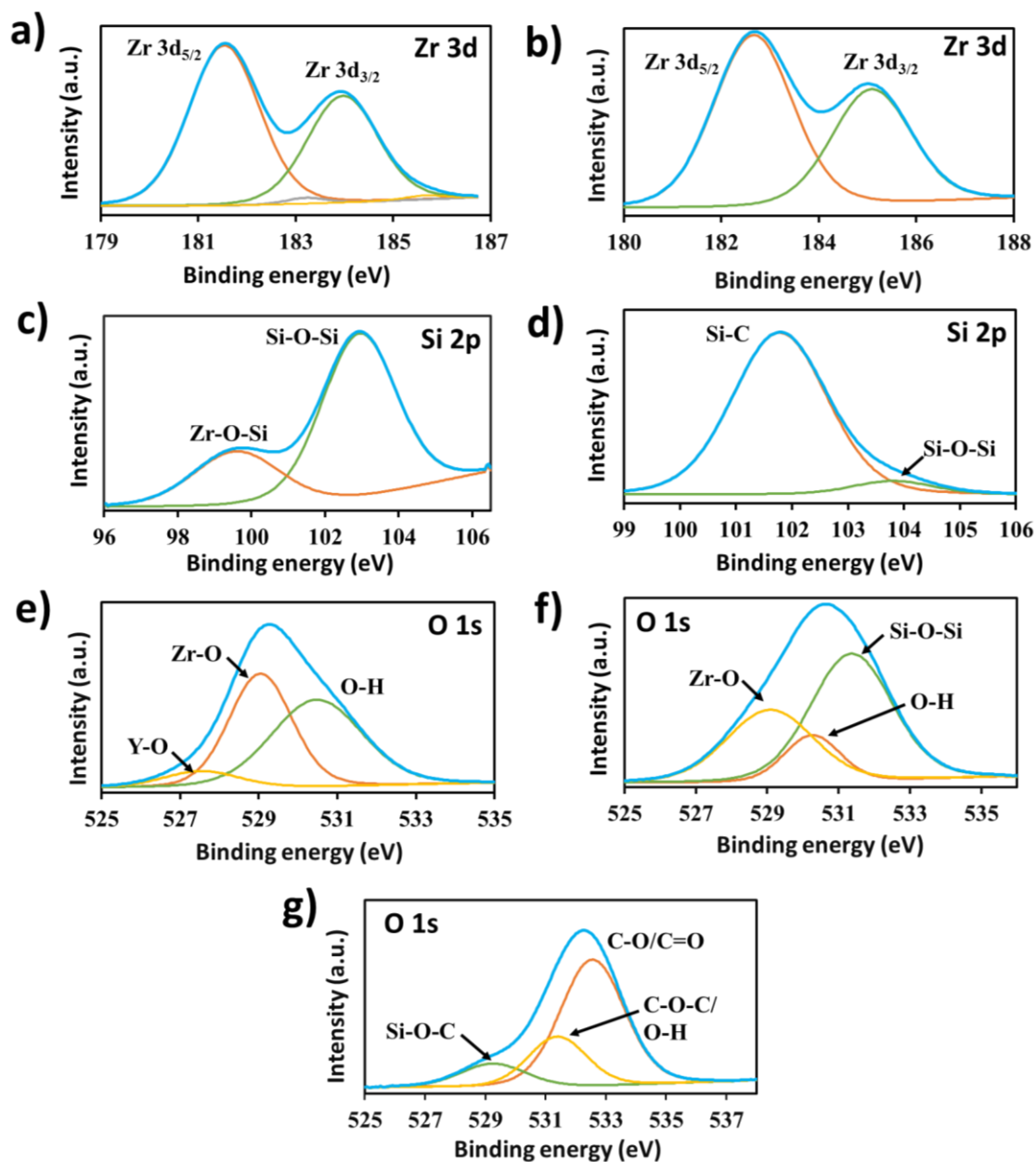


**Figure 3.** XPS high-resolution spectra of: (a, b) Zr 3d; (c, d) Si 2p 1; and (e- g) O 1s. Samples identification: 3D-printed zirconia platforms (a, e); 3D-printed zirconia with  $\gamma$ -MPS silane monolayer (b, c, f); and PICN scaffolds (d, g).

As a conclusion, the correlation among high-resolution spectra of Zr 3d, Si 2p and O 1s proves that  $\gamma$ -MPS is adhered to the zirconia surface, acting as coupling agent for the adhesion of the methacrylate copolymer resin. The survey spectrum for each sample is shown in Figure S3 and Table S2 lists the atomic percentage of Zr 3d, Si 2p, O 1s and C1s atoms.

The copolymer adhesion was investigated by Raman and SEM analyses. For this characterization the 40:60 Bis-GMA/TEGDMA ratio was chosen as the most suitable proportion for the zirconia pore infiltration. Figure 4a shows a 3D map of PICN side zone after cutting and polishing it, until a satisfying surface finishing was reached. The Raman image identifies the main regions in the cubic section of the sample with 40:60 Bis-GMA/TEGDMA copolymer. It clearly evidences the infiltration of the polymer inside of the pores. As it can be seen, the mapping analysis enables discrimination between the different components of the hybrid material according to their nature. The red colour represents the copolymer, while the green colour shows the single filaments of 3D-printed structure. Raman mapping analysis allowed the identification of the main absorption bands of the 40:60 Bis-GMA/TEGDMA copolymer and the 3Y-TZP zirconia scaffold is displayed in Figure 4b and 4c, respectively. The Raman shift of the copolymer was previously reported [60], and the main absorption bands are associated with C=C, C=O, =C-H and C-H groups. Furthermore, 3Y-TZP absorption bands from 100 to 1100  $\text{cm}^{-1}$  correspond to the standard representation of sintered 3Y-TZP zirconia reported in literature [61,62]. The 3Y-TZP sintered samples showed to adopt mostly the tetragonal phase with characteristic sharp bands of the different Raman modes at approximately 145, 263, 320, 465, 612, and 643  $\text{cm}^{-1}$  (Figure 4c). Complete characterization of the other copolymer ratios studied in the present work can be found in the supporting information (Figures S4, S5 and S6) and corroborates with previous report [63].

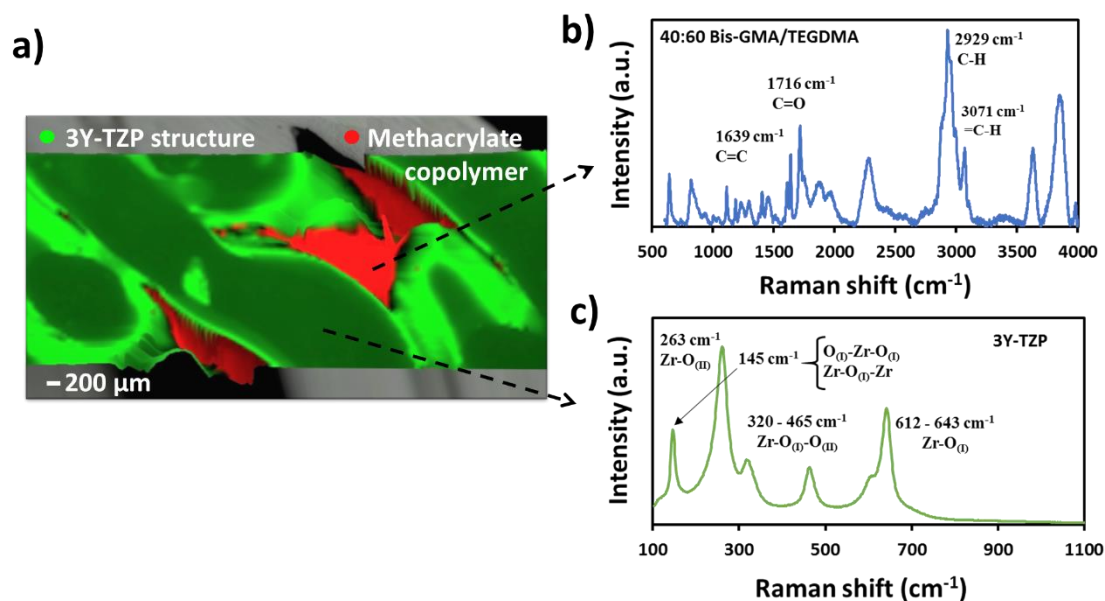


**Figure 4.** (a) Confocal 3D mapping of copolymer-infiltrated cubic sample (in green, are visible zirconia filaments and in red the copolymer inside of the pores). Raman spectra of: (b) the 40:60 Bis-GMA/TEGDMA copolymer, and (c) the 3Y-TZP zirconia structure.

As mentioned before, the main aim of this work was to achieve successful infiltration of ceramic scaffold with methacrylate resin to obtain stable structures for future dental applications. As well known, dental implants manufactured by ceramic material are generally considered to be hard and brittle in nature.[29] Ceramics can be toughened by reinforcement with other materials.[64,65] The polymer adhesive is intended to toughen the porous zirconia scaffold by reinforcing its filaments and amortize the impact or tensions generated over the long time-implanted prosthesis.

SEM micrographs displayed in Figure 5 demonstrate the properly infiltrated pores (Figure 5a) and the excellent adhesion in copolymer-zirconia interfaces (Figure 5b). The lack of gaps or vacancies at the interface points (Figure 5b) is observed, even after mechanical manipulation of the sample (cutting and polishing treatment). This result supports our strategy of silanization and further Bis-GMA/TEGDMA deposition for the

preparation of the PICN devices, in terms of two-stage synthesis and without additional surface activation. The proposed strategy represents an easy method to reinforce hollow 3D-printed zirconia scaffolds.

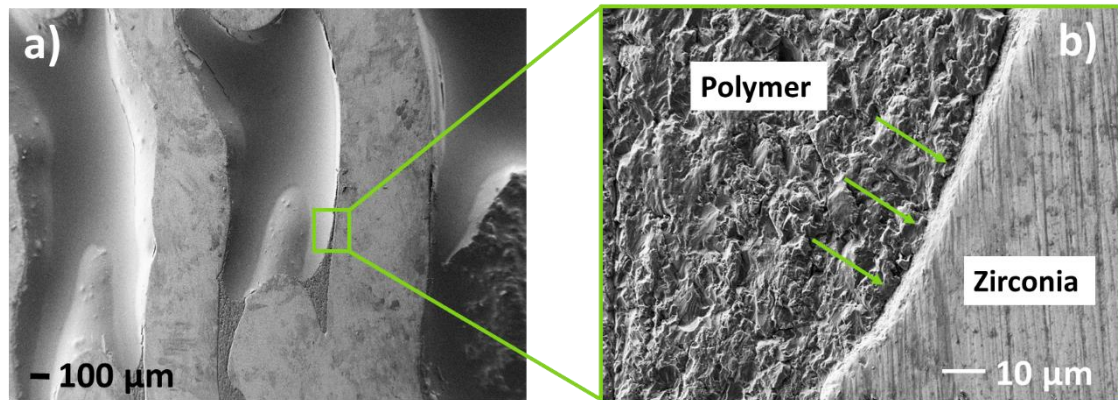


**Figure 5.** SEM micrographs of PICN samples, proving the adhesion and infiltration of pores by Bis-GMA/TEGDMA deposition after silanization: a) low magnification image of two infiltrated pores; and b) high magnification image of the polymer-ceramic interface.

### 3.3. Compression test

As mechanical performance of dental implant is an important aspect of a material design, the compression strength of specimen was measured. The compression strength of zirconia scaffolds was compared with PICN sample and also with a sample printed with 100% infill of zirconia filaments. The behaviour of specimens, while undergoing compression was recorded in the means of stress-strain curves, which are displayed in Figure 6. Due to the morphology of the 3D-printed cubic samples, it was not possible to obtain homogeneous height curves. Therefore, the data were recorded until a breakage or load limit of ~7 kN. There are a significant difference in between the three samples, as can be seen by the photographs from pieces after broken under pressure load (Figure 6, inset). In the case of zirconia scaffold without polymer infiltrated (Figure 6, blue curve), the cube loses its mechanical integrity at only 2.1 % of elongation at break ( $\epsilon$ ) and the

strength resistance diminishes. On the other hand, in the case of PICN samples, it resists to start breaking until 3 % of  $\epsilon$ , whereas the pieces resist the stress force applied (Figure 6, red curve). The drops along the curve show breakage of small parts of the PICN sample, especially in corners, but the core of the infiltrated sample stays undamaged even at 7 kN. This fact demonstrates that the mechanical properties can be compared with sample with 100% infill cubic structure (Figure 6, green curve).

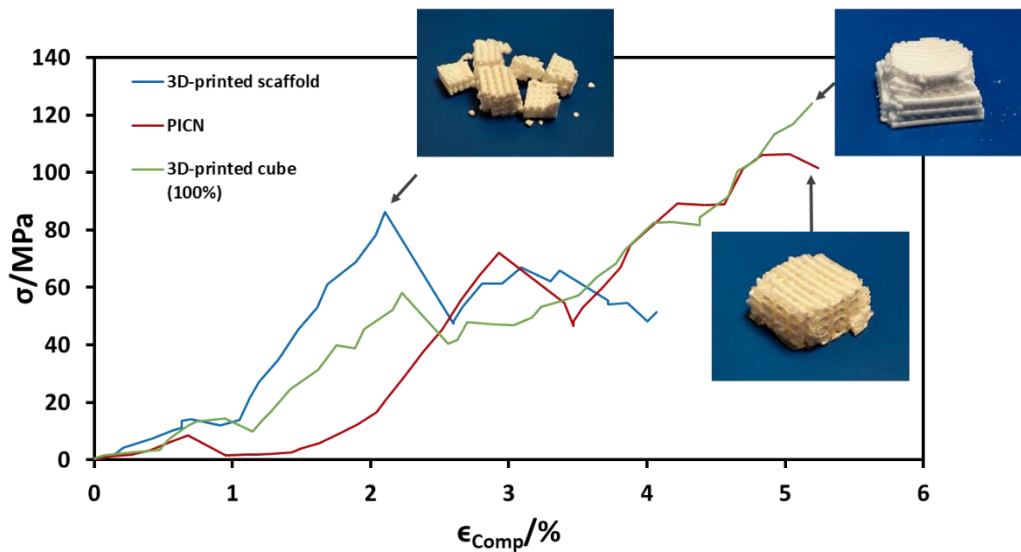


**Figure 6.** Stress-strain curves obtained after compression test, at 0.5 mm/s of pressure rate, for the 3D-printed zirconia scaffold, 3D-printed zirconia with copolymer infiltrated (PICN sample) and 3D-printed cube with 100 % infill of zirconia filaments. Insets: photographs taken after the pieces ruptures or until reach the pressure force of 7 kN.

### 3.4. Antimicrobial activity of PICN devices

In this study, we are combining three different materials: a zirconia substrate, an organic-inorganic anchoring molecule and a copolymer adhesive. Each one has different surface properties and different behaviour over bacteria proliferation. The organosilane compound is supposed to not be in direct contact with saliva, therefore, its bacterial property is of less importance. However, with time, saliva can penetrate to the abutment of zirconia and reach the titanium screw implants under the zirconia abutment.

*Streptococcus salivarius* is one of the microorganisms present on saliva and responsible for dental caries,[66] whereas *Escherichia coli* is the most commonly used type of gram negative bacterial line and is considered a model organism in microbiological studies.[67] Such microorganisms were chosen to evaluate the bacterial activity on the new material.

Therefore, to ensure the possible application of the new composite in the biomedical field, the antimicrobial activity and bacteria adhesion of all stages of the composite preparation were tested. Figure 7 summarizes the antimicrobial behaviour of each sample. The control, which was the same as for the proliferation or adhesion tests, consisted on bacteria seeded in sterile vials (*i.e.* without additional materials) using optimal conditions for promoting their growth. As expected, zirconia scaffolds showed lower bacterial growth than the control (Figure 7a), due to its inert structure, as previously reported by El-Ghany and Sherief [68]. On the other hand, 3D-printed scaffolds with  $\gamma$ -MPS silane monolayer and PICN samples did not experience significant changes after 24 h of bacteria incubation. However, the *S. salivarius* bacteria colonies rose slightly in this hydrophilic surface compared to the *E. coli* organisms and to the control (Figure 7a), showing a preference for this compound. By other hand, the error deviation is also high in *S. salivarius*, suggesting that such result should be taken carefully [52]. The 3D-printed structures with infiltrated polymer showed similar relative viability of bacteria growth in either *S. salivarius* or *E. coli* media.

By contrary, *E. coli* proliferation is higher in silane and copolymer surfaces than *S. salivarius* microorganisms (Figure 7b). It was also evidenced in the SEM images (Figures 8 and 9). Bacteria growth is favoured by the media, whereas bacteria adhesion depends on several factors: surface roughness, material hydrophilicity, presence of charges, superficial tension, and others. In general, the bacteria proliferation to the surface of any of the studied samples was found to be limited, the lowest values being obtained

for the 3D-printed zirconia substrate with Bis-GMA/TEGDMA copolymer coating ( $78.5 \pm 1.3 \%$  and  $61.6 \pm 5.2 \%$  in *E. coli* and *S. salivarius*, respectively). In the case of the zirconia scaffolds alone, the antimicrobial behaviour observed from growth and adhesion tests was similar.[68] However, the *S. salivarius* proliferation increases in 24 h due to the preference of such microorganism for roughness surfaces. The most roughness surface of zirconia filaments (Figure 2b) usually promotes microorganism adhesion compared to polymer smooth surfaces. After zirconia filaments covering with copolymer, such proliferation decreases (Figure 7b), proving that filaments are well recovered by the copolymer.

Careful evaluation of the copolymer samples allowed discrimination between *E. coli* and *S. salivarius*, the former showing a slight higher adhesion of *E. coli* bacteria than the latter. SEM micrographs of *E. coli* bacteria attached to the surface of the composite (Figures 8a-d) reveal that the copolymer forms a small valley between the filaments in which the colonies of bacteria are mostly accumulated. Another important observation is that bacteria can proliferate inside some of the superficial micropores of the zirconia filaments, supposedly not fully covered by the adhesive (Figure 8c, circle inside), making difficult their removal. If SEM micrographs at low magnification, from filaments and pores covered by the adhesive and incubated in *E. coli* and *S. salivarius*, respectively, are compared (Figures 8b and 9b), big colonies are mostly observed inside valleys. Thus, SEM images proves that the topography of the samples has a remarkable influence on the bacteria proliferation. Our results prove that the antimicrobial properties of 3Y-TZP infiltrated with Bis-GMA/TEGDMA are similar to those of pure zirconia, which make it a suitable hybrid material for the medical field [50,69]. Studies on cell proliferation and cell adhesion, with osteoblast MG-63 cells, to observe the biocompatibility of the new system are under progress.

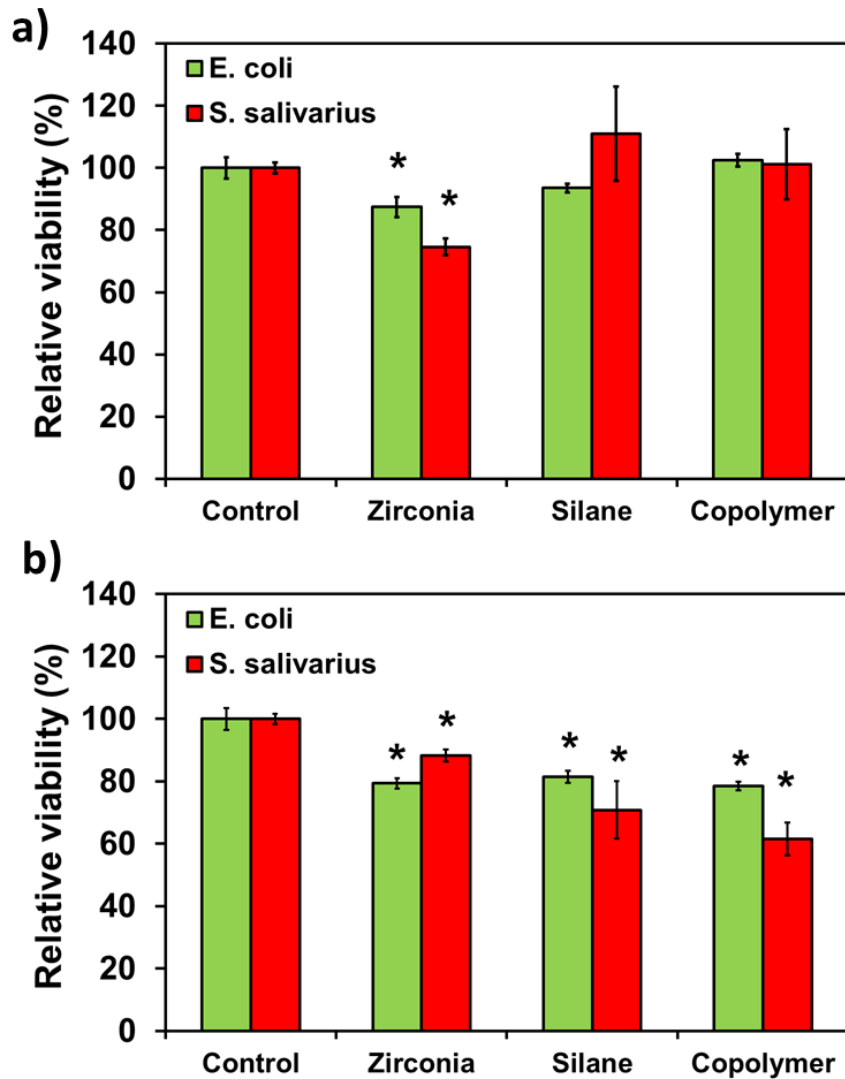


**Figure 7.** Antimicrobial activity of composites tested with *E. coli* and *S. salivarius* bacterial lines for plane zirconia scaffolds (marked as Zirconia), scaffolds coated with  $\gamma$ -MPS (marked as Silane) and PICN scaffolds (marked as Copolymer): a) bacterial growth and b) bacterial adhesion, both recorded after 24h. Results marked with stars are confidence level where  $p < 0.05$ , using the Student's T-test.

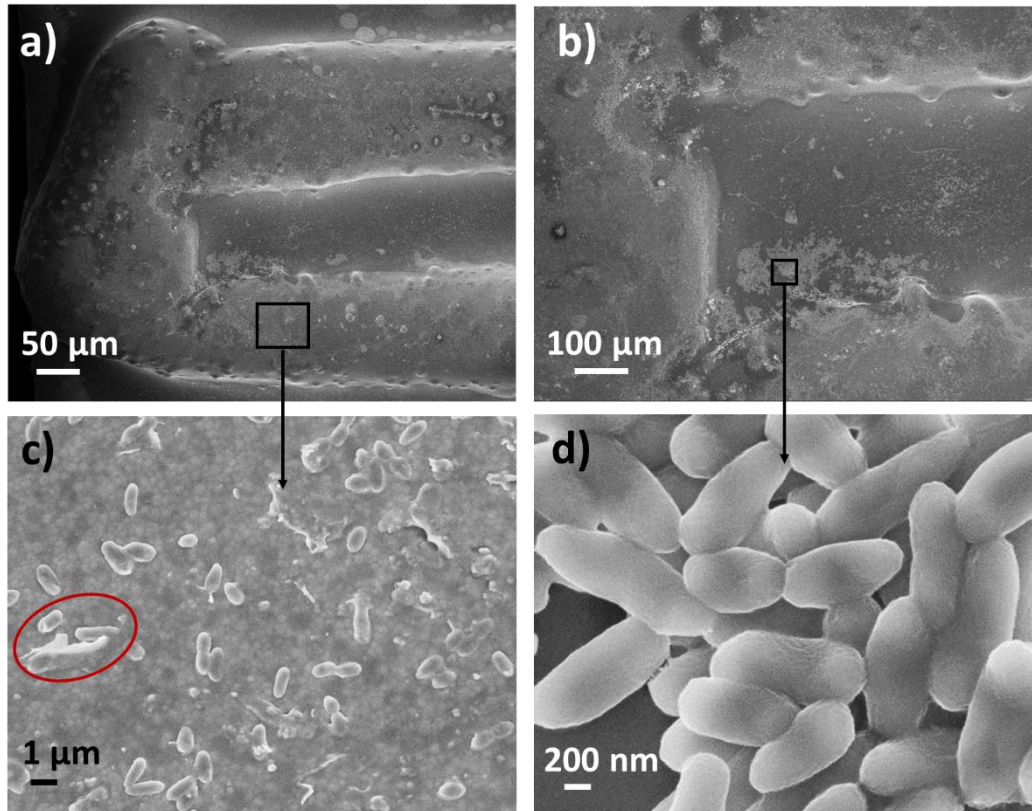


**Figure 8.** SEM micrographs of *E. coli* colony at the surface of PICN sample: a) overview of filaments and pores covered by copolymer (low magnification,  $\times 100$ ), b) higher magnification of image a) ( $\times 250$ ), c) microorganism growth on zirconia filaments ( $\times 10000$ ), and d) microorganism growth on scaffold pores ( $\times 50000$ ). The red circle in image c) shows one example of bacteria inside filament micropores.

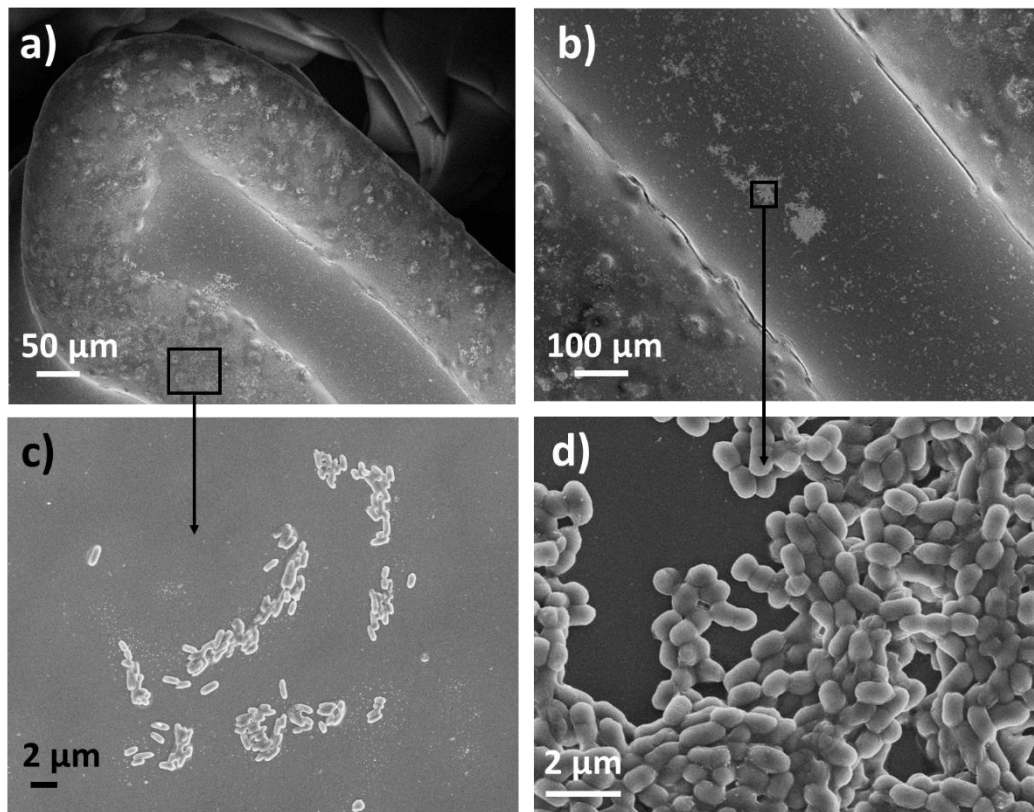


**Figure 9.** SEM micrographs of *S. salivarius* colony at the surface of PICN sample: a) overview of filaments and pores covered by copolymer (low magnification,  $\times 100$ ), b) higher magnification of image a) ( $\times 250$ ), c) microorganism growth on zirconia filaments ( $\times 5000$ ), and d) microorganism growth on scaffold pores ( $\times 15000$ ).

#### 4. Conclusions

In this work the feasibility fabrication of dimensionally stable and highly porous zirconia scaffolds (50 % of voids) by combining two technologies, robocasting manufacturing and polymer-infiltrated ceramic network, has been proved. The use of a high-tech 3D-printer, with precise control over the ink paste deposition was the key for the success achieved with cubic geometry processing and stability, containing  $49.98 \pm 2.75$  % of pores among ceramic filaments. After the sintering step, a reduction of only 20 % of the original printed dimensions, with no mismatch in the compactness of the ZrO<sub>2</sub> filaments was observed by digital images.

Another successful strategy was to promote the adhesion of Bis-GMA/TEGDMA copolymer (40:60 ratio) by previous functionalization of the 3Y-TZP filaments with  $\gamma$ -MPS organosilane compound. The pores of the 3D-printed scaffolds were almost completely filled, obtaining an infiltration density of  $87.50 \pm 6.56$  %, which is not possible to reach with conventional ceramic production methods. The filaments are well impregnated by the copolymer, as checked by optical and SEM analyses, and the polymer infiltrated scaffold is more resistant to filament rupture if compared to the non-infiltrated one, as demonstrated by the compression test.

The scaffold architecture plays an important role in bacteria adhesion and proliferation. The novel zirconia scaffolds prepared using polymer-infiltrated ceramic network and 3D-printing technologies exhibits antimicrobial properties similar to that of 3Y-TZP, as has been demonstrated by the adhesion and proliferation tests with *E. coli* and *S. salivarius* bacteria. This study is the preliminary approach to explore the cell viability and mechanical properties of the new scaffold composite for dental implants.

## Acknowledgements

This work has been co-funded by European Regional Development Fund (ERDF) from European Union, inside the regional operating program of Catalunya 2014-2020, with an import of 1.887.221,20€ (SIFECAT 001-P-001646), by MINECO and FEDER funds (RTI2018-098951-B-I00) and by Generalitat de Catalunya (2017SGR359 and 2017SGR0933). L. Hodasova acknowledges Universitat Politècnica de Catalunya for PhD fellowship (n° 6-CP\_SCSRE). C. Alemán acknowledges the “ICREA Academia 2015” award for excellence in research, funded by the Generalitat de Catalunya. The authors are grateful to Dr. L. Franco for her help with the thermal analysis.

## References

- [1] B. Berman, 3-D printing : The new industrial revolution, *Bus. Horiz.* 55 (2012) 155–162. doi:10.1016/j.bushor.2011.11.003.
- [2] B.T. Wittbrodt, A.G. Glover, J. Laureto, G.C. Anzalone, D. Oppliger, J.L. Irwin, J.M. Pearce, Life-cycle economic analysis of distributed manufacturing with open-source 3-D printers, *Mechatronics.* 23 (2013) 713–726. doi:10.1016/j.mechatronics.2013.06.002.
- [3] M. Kasparova, L. Grafova, P. Dvorak, T. Dostalova, A. Prochazka, H. Eliasova, Possibility of reconstruction of dental plaster cast from 3D digital study models, *Biomed. Eng. Online.* 12 (2013) 1–11.
- [4] J.W. Stansbury, M.J. Idacavage, 3D printing with polymers: Challenges among expanding options and opportunities, *Dent. Mater.* 32 (2016) 54–64. doi:10.1016/j.dental.2015.09.018.
- [5] L.C. Hwa, S. Rajoo, A.M. Noor, N. Ahmad, M.B. Uday, Recent advances in 3D printing of porous ceramics: A review, *Curr. Opin. Solid State Mater. Sci.* 21

- (2017) 323–347. doi:10.1016/j.cossms.2017.08.002.
- [6] G.B. Brown, G. Fräns Currier, O. Kadioglu, J.P. Kierlb, Accuracy of 3-dimensional printed dental models reconstructed from digital intraoral impressions, *Am. J. Orthod. Dentofac. Orthop.* 154 (2018) 733–739. doi:10.1016/j.ajodo.2018.06.009.
- [7] A. Dawood, B.M. Marti, V. Sauret-Jackson, A. Darwood, 3D printing in dentistry, *Br. Dent. J.* 219 (2015) 521–529. doi:10.1038/sj.bdj.2015.914.
- [8] M. Juneja, N. Thakur, D. Kumar, A. Gupta, B. Bajwa, P. Jindal, Accuracy in dental surgical guide fabrication using different 3-D printing techniques, *Addit. Manuf.* 22 (2018) 243–255. doi:10.1016/j.addma.2018.05.012.
- [9] A. Awad, F. Fina, A. Goyanes, S. Gaisford, A.W. Basit, 3D printing: Principles and pharmaceutical applications of selective laser sintering, *Int. J. Pharm.* 586 (2020) 119594. doi:10.1016/j.ijpharm.2020.119594.
- [10] K. Shah, D.J. Lee, Fabricating a screw-retained, complete arch, fixed implant prosthesis using selective metal laser sintering: A clinical report, *J. Prosthet. Dent.* 123 (2020) 373–378. doi:10.1016/j.prosdent.2019.01.013.
- [11] M. Antanasova, A. Kocjan, M. Hočevcar, P. Jevnikar, Influence of surface airborne-particle abrasion and bonding agent application on porcelain bonding to titanium dental alloys fabricated by milling and by selective laser melting, *J. Prosthet. Dent.* 123 (2020) 491–499. doi:10.1016/j.prosdent.2019.02.011.
- [12] S. Baumgartner, R. Gmeiner, J.A. Schönherr, J. Stampfl, Stereolithography-based additive manufacturing of lithium disilicate glass ceramic for dental applications, *Mater. Sci. Eng. C.* 116 (2020) 111180. doi:10.1016/j.msec.2020.111180.
- [13] J.A. Schönherr, S. Baumgartner, M. Hartmann, J. Stampfl, Stereolithographic additive manufacturing of high precision glass ceramic parts, *Materials (Basel)*.

- 13 (2020) 5–7. doi:10.3390/ma13071492.
- [14] F. Chen, H. Zhu, J.M. Wu, S. Chen, L.J. Cheng, Y.S. Shi, Y.C. Mo, C.H. Li, J. Xiao, Preparation and biological evaluation of ZrO<sub>2</sub> all-ceramic teeth by DLP technology, *Ceram. Int.* 46 (2020) 11268–11274. doi:10.1016/j.ceramint.2020.01.152.
- [15] J. Zhang, Q. Hu, S. Wang, J. Tao, M. Gou, Digital light processing based three-dimensional printing for medical applications, *Int. J. Bioprinting.* 6 (2020) 12–27. doi:10.18063/ijb.v6i1.242.
- [16] M. Goldberg, T. Obolkina, S. Smirnov, P. Protsenko, D. Titov, O. Antonova, A. Konovalov, E. Kudryavtsev, I. Sviridova, V. Kirsanova, N. Sergeeva, V. Komlev, S. Barinov, The Influence of Co Additive on the Sintering, Mechanical Properties, Cytocompatibility, and Digital Light Processing Based Stereolithography of 3Y-TZP-5Al<sub>2</sub>O<sub>3</sub> Ceramics, *Materials (Basel).* 13 (2020) 2789. doi:doi:10.3390/ma13122789.
- [17] J. Li, J. Hu, Y. Zhu, X. Yu, M. Yu, H. Yang, Surface roughness control of root analogue dental implants fabricated using selective laser melting, *Addit. Manuf.* 34 (2020) 101283. doi:10.1016/j.addma.2020.101283.
- [18] D. Zhang, E. Peng, R. Borayek, J. Ding, Controllable Ceramic Green-Body Configuration for Complex Ceramic Architectures with Fine Features, *Adv. Funct. Mater.* 29 (2019) 1–12. doi:10.1002/adfm.201807082.
- [19] A.C. Branco, R. Silva, T. Santos, H. Jorge, A.R. Rodrigues, R. Fernandes, S. Bandarra, I. Barahona, A.P.A. Matos, K. Lorenz, M. Polido, R. Colaço, A.P. Serro, C.G. Figueiredo-Pina, Suitability of 3D printed pieces of nanocrystalline zirconia for dental applications, *Dent. Mater.* 36 (2020) 442–455. doi:10.1016/j.dental.2020.01.006.

- [20] H.N. Chia, B.M. Wu, Recent advances in 3D printing of biomaterials, *J. Biol. Eng.* 9 (2015) 1–14. doi:10.1186/s13036-015-0001-4.
- [21] H.O.T. Ware, A.C. Farsheed, B. Akar, C. Duan, X. Chen, G. Ameer, C. Sun, High-speed on-demand 3D printed bioresorbable vascular scaffolds, *Mater. Today Chem.* 7 (2018) 25–34. doi:10.1016/j.mtchem.2017.10.002.
- [22] R.S. Brum, P.R. Monich, M.C. Fredel, G. Contri, S.D.A.S. Ramoa, R.S. Magini, C.A.M. Benfatti, Polymer coatings based on sulfonated-poly-ether-ether-ketone films for implant dentistry applications, *J. Mater. Sci. Mater. Med.* 29:132 (2018) 1 of 9. doi:10.1007/s10856-018-6139-0.
- [23] D. Zhang, W. Jonhson, T.S. Heng, Y.Q. Ang, L. Yang, S.C. Tan, E. Peng, H. He, J. Ding, A 3D-printing method of fabrication for metals, ceramics, and multi-materials using a universal self-curable technique for robocasting, *Mater. Horizons.* 7 (2020) 1083–1090. doi:10.1039/c9mh01690b.
- [24] R.D. Farahani, K. Chizari, D. Therriault, Three-dimensional printing of freeform helical microstructures: A review, *Nanoscale.* 6 (2014) 10470–10485. doi:10.1039/c4nr02041c.
- [25] M. Tilton, G.S. Lewis, H. Bok Wee, A. Armstrong, M.W. Hast, G. Manogharan, Additive manufacturing of fracture fixation implants: Design, material characterization, biomechanical modeling and experimentation, *Addit. Manuf.* 33 (2020) 101137. doi:10.1016/j.addma.2020.101137.
- [26] S.J. Bonsor, G.J. Pearson, *A clinical guide to applied dental materials*, Elsevier/Churchill Livingstone, 2013.
- [27] T. Maridurai, D. Balaji, S. Sagadevan, Synthesis and characterization of yttrium stabilized zirconia nanoparticles, *Mater. Res.* 19 (2016) 812–816. doi:10.1590/1980-5373-MR-2016-0196.

- [28] A. Jonhson, P. Sinthuprasirt, H. Fathi, S. Pollington, Current Glass-Ceramic Systems Used in Dentistry, in: S.H. Nandyala, J. Dos Santos (Eds.), *Curr. Trends Glas. Ceram. Mater.*, Bentham Science Publishers, Sharjak, 2013: pp. 49–72.  
[https://books.google.es/books?id=iKcVDgAAQBAJ&pg=PA58&lpg=PA58&dq=spinel+blank+ceramic&source=bl&ots=H25bvtewWx&sig=ACfU3U0rce8GmtCXHEB1fg8xLIm-cNjgrw&hl=es&sa=X&ved=2ahUKEwiT053arYHqAhUK8hQKHYZmBMsQ6AEwEnoECAYQAQ#v=onepage&q=spinel blank ceramic&f=false](https://books.google.es/books?id=iKcVDgAAQBAJ&pg=PA58&lpg=PA58&dq=spinel+blank+ceramic&source=bl&ots=H25bvtewWx&sig=ACfU3U0rce8GmtCXHEB1fg8xLIm-cNjgrw&hl=es&sa=X&ved=2ahUKEwiT053arYHqAhUK8hQKHYZmBMsQ6AEwEnoECAYQAQ#v=onepage&q=spinel%20blank%20ceramic&f=false) (accessed June 14, 2020).
- [29] J.W. Adams, R. Ruh, K.S. Mazdiyasi, Young's Modulus, Flexural Strength, and Fracture of Yttria-Stabilized Zirconia versus Temperature, *J. Am. Ceram. Soc.* 80 (1997) 903–908.
- [30] J. Li, X.H. Zhang, B.C. Cui, Y.H. Lin, X.L. Deng, M. Li, C.W. Nan, Mechanical performance of polymer-infiltrated zirconia ceramics, *J. Dent.* 58 (2017) 60–66.  
doi:10.1016/j.jdent.2017.01.008.
- [31] K. Srigurunathan, R. Meenambal, A. Guleria, D. Kumar, J.M.D.F. Ferreira, S. Kannan, Unveiling the Effects of Rare-Earth Substitutions on the Structure, Mechanical, Optical, and Imaging Features of ZrO<sub>2</sub> for Biomedical Applications, *ACS Biomater. Sci. Eng.* 5 (2019) 1725–1743.  
doi:10.1021/acsbiomaterials.8b01570.
- [32] M. Guazzato, M. Albakry, L. Quach, M. V. Swain, Influence of surface and heat treatments on the flexural strength of a glass-infiltrated alumina/zirconia-reinforced dental ceramic, *Dent. Mater.* 21 (2005) 454–463.  
doi:10.1016/j.dental.2004.07.010.
- [33] L.-H. He, M. Swain, A novel polymer infiltrated ceramic dental material, *Dent.*

- Mater. 27 (2011) 527–534. doi:10.1016/j.dental.2011.02.002.
- [34] A. Coldea, M. V. Swain, N. Thiel, In-vitro strength degradation of dental ceramics and novel PICN material by sharp indentation, *J. Mech. Behav. Biomed. Mater.* 26 (2013) 34–42. doi:10.1016/j.jmbbm.2013.05.004.
- [35] A. Coldea, M. V. Swain, N. Thiel, Mechanical properties of polymer-infiltrated-ceramic-network materials, *Dent. Mater.* 29 (2013) 419–426. doi:10.1016/j.dental.2013.01.002.
- [36] M. V. Swain, A. Coldea, A. Bilkhair, P.C. Guess, Interpenetrating network ceramic-resin composite dental restorative materials, *Dent. Mater.* 32 (2016) 34–42. doi:10.1016/j.dental.2015.09.009.
- [37] J.E. Smay, G.M. Gratson, R.F. Shepherd, J. Cesarano, J.A. Lewis, Directed colloidal assembly of 3D periodic structures, *Adv. Mater.* 14 (2002) 1279–1283. doi:10.1002/1521-4095(20020916)14:18<1279::AID-ADMA1279>3.0.CO;2-A.
- [38] D. Therriault, R.F. Shepherd, S.R. White, J.A. Lewis, Fugitive inks for direct-write assembly of three-dimensional microvascular networks, *Adv. Mater.* 17 (2005) 395–399. doi:10.1002/adma.200400481.
- [39] I.D. Sideridou, M.M. Karabela, Effect of the amount of 3-methacyloxypropyltrimethoxysilane coupling agent on physical properties of dental resin nanocomposites, *Dent. Mater.* 25 (2009) 1315–1324. doi:10.1016/j.dental.2009.03.016.
- [40] B. Chen, Z. Lu, H. Meng, Y. Chen, L. Yang, H. Zhang, H. Xie, C. Chen, Effectiveness of pre-silanization in improving bond performance of universal adhesives or self-adhesive resin cements to silica-based ceramics: Chemical and in vitro evidences, *Dent. Mater.* 35 (2019) 543–553. doi:10.1016/j.dental.2019.01.010.

- [41] A.I. Hussein, Bacterial Adhesion on Zirconia, Lithium Desilicated and Gold Crowns-In Vivo Study, *Adv. Dent. Oral Heal.* 1 (2016) 105–107.  
doi:10.19080/adoh.2016.01.555574.
- [42] M. Kumaresan, K. Vijai Anand, K. Govindaraju, S. Tamilselvan, V. Ganesh Kumar, Seaweed *Sargassum wightii* mediated preparation of zirconia (ZrO<sub>2</sub>) nanoparticles and their antibacterial activity against gram positive and gram negative bacteria, *Microb. Pathog.* 124 (2018) 311–315.  
doi:10.1016/j.micpath.2018.08.060.
- [43] A. Accardo, M.C. Blatché, R. Courson, I. Loubinoux, C. Thibault, L. Malaquin, C. Vieu, Multiphoton Direct Laser Writing and 3D Imaging of Polymeric Freestanding Architectures for Cell Colonization, *Small.* 13 (2017) 1–11.  
doi:10.1002/sml.201700621.
- [44] J. Schweiger, D. Bomze, M. Schwentenwein, 3D Printing of Zirconia—What is the Future?, *Curr. Oral Heal. Reports.* 6 (2019) 339–343. doi:10.1007/s40496-019-00243-4.
- [45] F.S.L. Bobbert, A.A. Zadpoor, Effects of bone substitute architecture and surface properties on cell response, angiogenesis, and structure of new bone, *J. Mater. Chem. B.* 5 (2017) 6175–6192. doi:10.1039/c7tb00741h.
- [46] V. Dalmoro, J.H.Z. dos Santos, E. Armelin, C. Alemán, D.S. Azambuja, A synergistic combination of tetraethylorthosilicate and multiphosponic acid offers excellent corrosion protection to AA1100 aluminum alloy, *Appl. Surf. Sci.* 273 (2013) 758–768. doi:10.1016/j.apsusc.2013.02.131.
- [47] J.I. Iribarren-Mateos, I. Buj-Corral, J. Vivancos-Calvet, C. Alemán, J.I. Iribarren, E. Armelin, Silane and epoxy coatings: A bilayer system to protect AA2024 alloy, *Prog. Org. Coatings.* 81 (2015) 47–57.

- doi:10.1016/j.porgcoat.2014.12.014.
- [48] V. Dalmoro, D.S. Azambuja, C. Alemán, E. Armelin, Hybrid organophosphonic-silane coating for corrosion protection of magnesium alloy AZ91: The influence of acid and alkali pre-treatments, *Surf. Coatings Technol.* 357 (2019) 728–739. doi:10.1016/j.surfcoat.2018.10.013.
- [49] V. Dalmoro, C. Alemán, C.A. Ferreira, J.H.Z. Dos Santos, D.S. Azambuja, E. Armelin, The influence of organophosphonic acid and conducting polymer on the adhesion and protection of epoxy coating on aluminium alloy, *Prog. Org. Coatings.* 88 (2015) 181–190. doi:10.1016/j.porgcoat.2015.07.004.
- [50] C. Caravaca, L. Shi, S. Balvay, P. Rivory, E. Laurenceau, Y. Chevolot, D. Hartmann, L. Gremillard, J. Chevalier, Direct silanization of zirconia for increased biointegration, *Acta Biomater.* 46 (2016) 323–335. doi:10.1016/j.actbio.2016.09.034.
- [51] M. Cadenaro, T. Maravic, A. Comba, A. Mazzoni, L. Fanfoni, T. Hilton, J. Ferracane, L. Breschi, The role of polymerization in adhesive dentistry, *Dent. Mater.* 35 (2019) 1–22. doi:10.1016/j.dental.2018.11.012.
- [52] J.P. Matinlinna, C.Y.K. Lung, J.K.H. Tsoi, Silane adhesion mechanism in dental applications and surface treatments: A review, *Dent. Mater.* 34 (2018) 13–28. doi:10.1016/j.dental.2017.09.002.
- [53] X. Yue, X. Hou, J. Gao, P. Bao, J. Shen, Effects of MDP-based primers on shear bond strength between resin cement and zirconia, *Exp. Ther. Med.* 17 (2019) 3564–3572. doi:10.3892/etm.2019.7382.
- [54] T. Yamauchi, H. Kitamura, N. Wakai, S. Zaima, Y. Koide, Y. Yasuda, Photoelectron spectroscopic studies on interfacial reactions in Zr/2×1(100) Si and Zr/SiO<sub>2</sub>/(100) Si systems, *J. Vac. Sci. Technol. A Vacuum, Surfaces, Film.* 11

- (1993) 2619–2622. doi:10.1116/1.578616.
- [55] I. Milošev, Ž. Jovanović, J.B. Bajat, R. Jančić-Heinemann, V.B. Mišković-Stanković, Surface Analysis and Electrochemical Behavior of Aluminum Pretreated by Vinyltriethoxysilane Films in Mild NaCl Solution, *J. Electrochem. Soc.* 159 (2012) C303–C311. doi:10.1149/2.042207jes.
- [56] J.M. Oliveira, T. Miyazaki, M.A. Lopes, C. Ohtsuki, J.D. Santos, Bonelike®/PLGA hybrid materials for bone regeneration: Preparation route and physicochemical characterisation, *J. Mater. Sci. Mater. Med.* 16 (2005) 253–259. doi:10.1007/s10856-005-6687-y.
- [57] M.E. Simonsen, C. Sønderby, Z. Li, E.G. Sjøgaard, XPS and FT-IR investigation of silicate polymers, *J. Mater. Sci.* 44 (2009) 2079–2088. doi:10.1007/s10853-009-3270-9.
- [58] M.R. Turner, E. Duguet, C. Labrugère, Characterization of silane-modified ZrO<sub>2</sub> powder surfaces, *Surf. Interface Anal.* 25 (1997) 917–923. doi:10.1002/(SICI)1096-9918(199711)25:12<917::AID-SIA314>3.0.CO;2-3.
- [59] B. Sivaranjini, R. Mangaiyarkarasi, V. Ganesh, S. Umadevi, Vertical Alignment of Liquid Crystals over a Functionalized Flexible Substrate, *Sci. Rep.* 8 (2018) 1–13. doi:10.1038/s41598-018-27039-3.
- [60] J. Xu, I.S. Butler, D.F.R. Gibson, I. Stangel, High-pressure infrared and FT-Raman investigation of a dental composite, *Biomaterials.* 18 (1997) 1653–1657. doi:10.1016/S0142-9612(97)00123-3.
- [61] Q. Wang, C. Li, M. Guo, C. Hu, Y. Xie, Controllable synthesis of zirconia nanopowders using vapor-phase hydrolysis and theoretical analysis, *J. Mater. Chem. A.* 2 (2014) 1346–1352. doi:10.1039/c3ta13571c.
- [62] A. Ghosh, A.K. Suri, M. Pandey, S. Thomas, T.R. Rama Mohan, B.T. Rao,

- Nanocrystalline zirconia-yttria system-a Raman study, *Mater. Lett.* 60 (2006) 1170–1173. doi:10.1016/j.matlet.2005.10.102.
- [63] F. Alifui-Segbaya, J. Bowman, A.R. White, R. George, I. Fidan, R.M. Love, Chemical characterization of additively manufactured methacrylates for dental devices, *Addit. Manuf.* 31 (2020) 100944. doi:10.1016/j.addma.2019.100944.
- [64] T. Yu, Z. Zhang, Q. Liu, R. Kuliiev, N. Orlovskaya, D. Wu, Extrusion-based additive manufacturing of yttria-partially-stabilized zirconia ceramics, *Ceram. Int.* 46 (2020) 5020–5027. doi:10.1016/j.ceramint.2019.10.245.
- [65] C.H. Lin, Y.M. Lin, Y.L. Lai, S.Y. Lee, Mechanical properties, accuracy, and cytotoxicity of UV-polymerized 3D printing resins composed of Bis-EMA, UDMA, and TEGDMA, *J. Prosthet. Dent.* 123 (2020) 349–354. doi:10.1016/j.prosdent.2019.05.002.
- [66] C.G. Figueiredo-Pina, M. Guedes, J. Sequeira, D. Pinto, N. Bernardo, C. Carneiro, On the influence of *Streptococcus salivarius* on the wear response of dental implants: An in vitro study, *J. Biomed. Mater. Res. - Part B Appl. Biomater.* 107 (2019) 1393–1399. doi:10.1002/jbm.b.34231.
- [67] C.J. Chen, S.J. Ding, C.C. Chen, Effects of surface conditions of titanium dental implants on bacterial adhesion, *Photomed. Laser Surg.* 34 (2016) 379–388. doi:10.1089/pho.2016.4103.
- [68] O.S. Abd El-Ghany, A.H. Sherief, Zirconia based ceramics, some clinical and biological aspects: Review, *Futur. Dent. J.* 2 (2016) 55–64. doi:10.1016/j.fdj.2016.10.002.
- [69] D. Mostafa, M. Aboushelib, Bioactive–hybrid–zirconia implant surface for enhancing osseointegration: an in vivo study, *Int. J. Implant Dent.* 4 (2018). doi:10.1186/s40729-018-0129-3.

# Graphical Abstract

